Angewandte Chemie International Edition

Angewandte International Edition Chemie

How to cite: *Angew. Chem. Int. Ed.* **2026**, e1821803
doi.org/10.1002/anie.1821803

RESEARCH ARTICLE

Anion-Managing Biomimetic Electrolyte Based on Fluorinated COF Recognition and Hyperbranched Polyamidoamine Capture for Practical Lithium–Metal Batteries

Jiazhu Guan[1,2] | Yu Zhang[1] | Yong Cao[1] | Yajuan Zhou[1] | Wenping Liu[1] | Qinghui Zeng[1] | Zhengyan Lun[1] | Wei Liu[1] | Shi Wang[2,3] | Wei Cui[1] | Zhong Jin[2] | Liaoyun Zhang[1]

[1]School of Chemical Sciences, University of Chinese Academy of Sciences, Beijing, China | [2]State Key Laboratory of Coordination Chemistry, MOE Key Laboratory of Mesoscopic Chemistry, MOE Key Laboratory of High Performance Polymer Materials and Technology, Jiangsu Key Laboratory of Advanced Organic Materials, Suzhou Key Laboratory of Green Intelligent Manufacturing of New Energy Materials and Devices, Tianchang New Materials and Energy Technology Research Center, Institute of Green Chemistry and Engineering, School of Chemistry and Chemical Engineering, Nanjing University, Nanjing, Jiangsu, China | [3]State Key Laboratory of Flexible Electronics (LoFE) & Institute of Advanced Materials (IAM), Nanjing University of Posts & Telecommunications, Nanjing, China

Correspondence: Shi Wang (iamshiwang@njupt.edu.cn) | Wei Cui (cuiwei@ucas.ac.cn) | Zhong Jin (zhongjin@nju.edu.cn) | Liaoyun Zhang (zhangly@ucas.edu.cn)

Received: 17 April 2026 | **Revised:** 30 June 2026 | **Accepted:** 14 July 2026

Keywords: biomimetic "recognition-capture" strategy | gradient interphase | hyperbranched polyamidoamine | solid polymer electrolytes

ABSTRACT

Solid polymer electrolytes (SPEs) hold great promise for next-generation high-safety lithium batteries, yet their development is fundamentally constrained by the inherent dilemma of poor ion transport and unstable electrode–electrolyte interfaces. To address the challenge, the biomimetic ion-management strategy termed "recognition-capture" strategy, inspired by the synergistic predation behavior of grouper and moray eel, is proposed. The covalent organic framework (COF) with ordered nanochannels is designed as the "moray eel" to recognize, enrich, and guide $TFSI^-$ anions, while the hyperbranched polyamidoamine (PAMAM) with dense amine groups serves as the "grouper" to deeply anchor and lock the anions. Therefore, the created composite electrolyte TFPL simultaneously achieves ionic conductivity of 4.5 mS cm^{-1} and t_{Li+} of 0.7. Moreover, the biomimetic "recognition-capture" strategy induces the spontaneous formation of the stable gradient interphase (Li_3N—Li_2S—LiF/LiH), which homogenizes Li^+ flux and suppresses dendrite. Consequently, Li||Li cells achieve stable cycling exceeding 1800 h. The TFPL electrolyte enables LFP cells to cycle stably for 450 cycles at 5 C, delivers over 240 mAh g^{-1} for NCM811 cell at 4.5 V, and offers 9.37 mAh for NCM523 pouch cells at 0.1 C. The strategy also proves effective in Li—S cell, demonstrating the broad applicability for next-generation solid-state lithium–metal batteries.

Jiazhu Guan and Yu Zhang contributed equally to this work.

1 | Introduction

With the rapid development of electric vehicles and large-scale energy storage technologies, the development of electrochemical energy storage systems with high energy density and high safety has become an urgent demand in the energy field [1–3]. Lithium–metal batteries (LMBs), which employ metallic lithium anodes with ultra-high specific capacity (3860 mAh g^{-1}) [4] and the lowest electrochemical potential (−3.04 V vs. standard hydrogen electrode) [5–7], are regarded as one of the ideal systems for achieving breakthroughs in energy density [8, 9]. However, side reactions between traditional liquid electrolytes and lithium–metal anodes and lithium dendrite severely restrict the practical application [10, 11]. Meanwhile, flammable organic electrolytes also pose significant safety hazards [12, 13]. As the solution integrating high safety and excellent processability, solid polymer electrolytes (SPEs) have attracted extensive attention [14, 15].

Currently, the research on SPEs mainly focuses on linear polymer electrolyte including polyethylene oxide (PEO) SPEs [16, 17], polycarbonate (PC) [18, 19] SPEs, fluorinated polymer [20, 21] SPEs, and linear polyacrylonitrile [17] SPEs, all of which have long been constrained by the classic "interlocking dilemma". Among linear polymer electrolytes, amide-containing polymers can immobilize anions via hydrogen-bond interactions and restrict anion migration [22–25]. Nevertheless, compared with hyperbranched counterparts, such linear macromolecules possess fewer amide sites and weaker anion adsorption capacity. In addition, the slow segmental dynamics of polymer chains further degrade ionic conductivity, making these materials unsuitable for practical applications [26]. Ye et al. developed a self-healing polyurethane electrolyte with an ionic conductivity of only 4.13×10^{-4} S cm^{-1} [27]. In addition, although several novel polymer electrolytes represented by ionic liquid-based systems deliver satisfactory ionic conductivity, the absence of amide bonds to immobilize migrating anions leads to a low lithium-ion transference number, thereby introducing safety risks to batteries. Fu et al. [28]. fabricated polymer electrolytes based on polymeric ionic liquids and ionic liquid plasticizers, which achieved a high room-temperature ionic conductivity of 0.8 mS cm^{-1}; nevertheless, the lithium-ion transference number is only 0.44.

To enhance the room-temperature ionic conductivity (σ), it is necessary to promote lithium salt dissociation and reduce the barrier of segmental motion, but this inevitably grants a high degree of migration freedom to anions (e.g., $TFSI^-$) [19]. The free migration of anions easily triggers severe polarization of concentration gradients, which not only directly lowers the apparent lithium-ion transference number (t_{Li+}), but also facilitates generation of lithium dendrite [29]. Meanwhile, the anions migrating to the electrode surface are prone to undergo continuous reductive/oxidative decomposition [30, 31], and the decomposition products easily form the fragile organic interphase layer with poor mechanical strength and low ion conduction ability [12], which is not conducive to effectively suppressing the recurrent interfacial side reactions [15].

To address this core challenge, existing research follows two conventional approaches: "suppression" or "blocking" of anion migration. The first approach involves incorporating inorganic fillers such as SiO_2 [32], Al_2O_3 [33], and LLZO [34, 35] into the polymer matrix that aim to leverage the filler to promote lithium salt dissociation, inhibit crystallization, and thereby enhance σ [13]. This approach has achieved noticeable improvements in ionic conductivity, yet it remains difficult to precisely regulate anion migration and interfacial reactions [36]. The other approach is to design single-ion conductors, where anions are permanently anchored to the polymer backbone via covalent bonds, aiming to fundamentally eliminate anion migration. Although the approach can achieve the theoretical t_{Li+} approaching 1 [37, 38], the strong covalent anchoring severely restricts the mobility of polymer segments [2, 39]. Therefore, simultaneously achieving high σ, high t_{Li+}, and high interfacial stability has become the core issue restricting the practical application of SPEs.

In the marine ecosystem, moray eels identify prey hiding in rocky crevices and flush them out, while groupers lying in ambush in open waters intercept and capture those prey. Inspired by the synergistic predation behavior of grouper and moray eel, we propose a biomimetic "recognition-capture" strategy and successfully fabricate a solid-state composite polymer electrolyte TFPL based on fluorine-containing covalent organic frameworks (COFs) and hyperbranched polyurea prepared by the polymerization of the hyperbranched polyamidoamine (PAMAM), polyetheramine (PEA), and isophorone diisocyanate (IPDI).

The strong electron-withdrawing —CF_3 groups of fluorinated COFs (Tp-TFMB) act as "moray eel", which function similarly to moray eel and are capable of "recognizing" and electrostatically repelling $TFSI^-$ anions. Meanwhile, the precisely engineered amide cavities provided by PAMAM serve as "grouper", which are analogous to the capture and enrichment functions of grouper, achieve specific capture and robust confinement of the anions migrating to the cavities. The process of "recognition–repulsion–capture" accurately imitate the efficient regulation of biological systems toward foreign substances, enabling directional transport, and regional confinement of anions in the TFPL. The design alleviates the dilemma that σ and t_{Li+} cannot be improved simultaneously and synchronously elevates the σ and t_{Li+} to 4.5 mS cm−^{1} and 0.7, respectively. More importantly, the design guides the ordered reconstruction of the electrode/electrolyte interface, which spontaneously forms the gradient interphase layer with both highly stable composition and structure. The cells assembled with created TFPL exhibit favorable and universal electrochemical performance. The LFP cells can achieve stable cycling for up to 450 cycles at 5 C and 1000 cycles at 1 C, while the multi-layer pouch cells also deliver the discharge capacity of 41 mAh at 0.1 C for 50 cycles with nearly zero capacity decay. Furthermore, the cells assembled with TFPL display discharge specific capacity of over 240 mAh g^{-1} at 4.5 V when paired with NCM811 cathodes. The assembled commercial NCM523 pouch cells operate stably for 40 cycles with high discharge capacity of 9.37 mAh. In addition, the strategy has been successfully extended to lithium–sulfur (Li—S) battery, confirming the broad application potential.

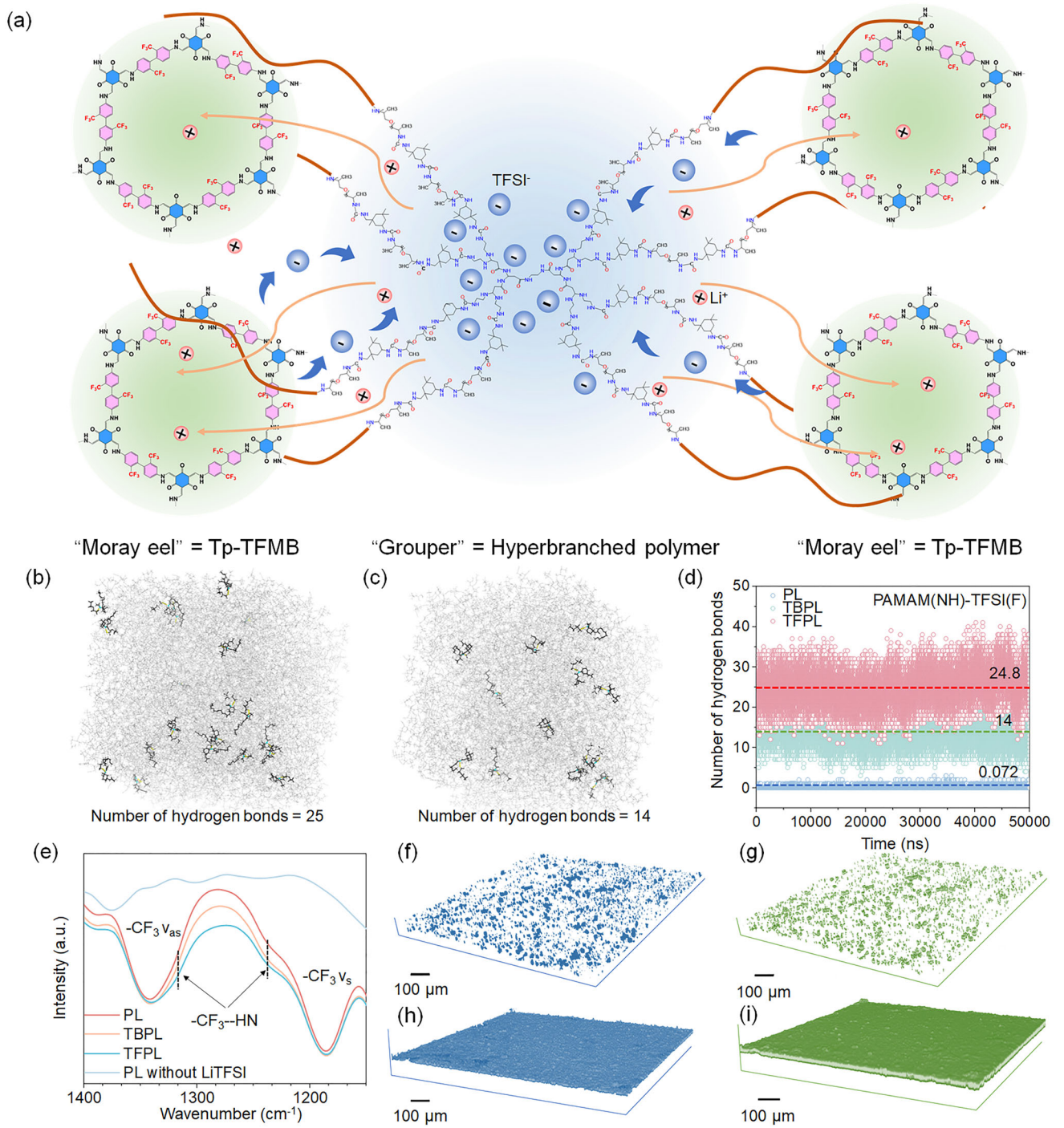

FIGURE 1 | (a) Schematic diagram of biomimetic "recognition–capture" synergistic strategy for anion trapping and fast lithium-ion transport; snapshot of the number of hydrogen bonds of (b) TFPL and (c) TBPL; (d) Number of hydrogen bonds between —NH on PAMAM and F on TFSI anions in PL, TBPL, and TFPL; (e) FTIR spectra of PL, TBPL, TFPL and PL without LiTFSI (1400 cm^{-1}–1150 cm^{-1}); Confocal laser scanning microscopy (CLSM) 3D images of PL at 405 nm (f) and 488 nm (g) wavelengths and TFPL at 405 nm (h) and 488 nm (i) wavelengths.

2 | Results and Discussion

2.1 | Biomimetic "Recognition–Capture" Synergistic System

As shown in Figure 1a, the biomimetic "recognition–capture" synergistic strategy is proposed, which is realized by constructing the composite electrolyte TFPL consisting of hyperbranched polymer, LiTFSI, and Tp-TFMB. Among them, the hyperbranched polymers are obtained via the polymerization reaction of amino groups of generation 2 polyamidoamine (PAMAM) and PEA with isophorone diisocyanate (IPDI). The optimal ratios are identified as precursor polymer: LiTFSI = 1:1.6 labeled as PL. To optimize the internal composition, a series of PL and Tp-TFMB-incorporated composite electrolytes TFPL with varying component ratios are screened via impedance and lithium-ion

transference number measurements. The optimal ratios are identified as precursor polymer: LiTFSI: Tp-TFMB = 1:1.6:0.01 named as TFPL (Figures S11–S14). Within this TFPL, PAMAM by virtue of the internal high-density amide bonds that enable precise capture and anchoring of bis(trifluoromethanesulfonyl)imide ($TFSI^-$) anions through multiple hydrogen bonds with —CONH— from PAMAM. Meanwhile, the abundant —CF_3 groups in Tp-TFMB can specifically expel $TFSI^-$ anions and drive anions enrichment toward the PAMAM region. Therefore, spatial preorganization and directional transport of anions are achieved. In addition, the hyperbranched structure of the polyurea network provides rapid transport channels for lithium ions (Li^+). This spatial and functional division of labor between "moray eel-driven migration" and "grouper-confined capture" allows full-process management of anions from recognition and transport to immobilization.

The molecular dynamics (MD) simulation is utilized to elucidate the synergistic mechanism of the biomimetic "recognition–capture" strategy at the molecular dynamics level. As illustrated in Figure 1b,c, the number of hydrogen bonds existing within the TFPL exceeds that within the TBPL, which contains PAMAM, PEA, LiTFSI, and TpBd without -CF_3. The results in Figure 1d reveal that the average number of hydrogen bonds (AHBs) formed between the amide bonds of PAMAM and the —CF_3 of $TFSI^-$ within the PL system is merely 0.072 over the simulation duration of 50 000 ns. Remarkably, the AHBs increase dramatically to 14 in the TBPL system incorporated with TpBd. The enhancement is primarily attributed to the steric hindrance effect induced by the structure of TpBd, which restricts the long-range migration of $TFSI^-$ anions, and thus elevates the probability of interaction with the PAMAM "cages". Nevertheless, the real breakthrough is achieved in the TFPL system modified with Tp-TFMB, where the AHBs further surge to 24.8. The substantial increase demonstrates that Tp-TFMB does not merely act as a passive barrier. Instead, the abundant —CF_3 effectively recognizes and drives more anions to migrate directionally and accumulate toward the PAMAM "cages" through stronger hydrogen interactions between $TFSI^-$ and amide in PAMAM.

Meanwhile, the Fourier transform infrared (FTIR) spectroscopy characterized the reconstruction of the hydrogen bond network in the TFPL. On the one hand, the C—N stretching vibration peaks of the amide and the —NH_2 vibration peaks of the amino in the PL, TBPL, and TFPL undergo blue-shift compared to PL without LiTFSI in Figures S4 and S5. On the other hand, the asymmetric stretching vibration peaks of —CF_3 and the characteristic peaks of —SO_2— derive from LiTFSI exhibit significant red-shift in Figures 1e and S5. The shifting trend collectively indicates the formation of strong hydrogen bonding interactions between the anions and the polymer.

Particularly important, the new shoulder peaks appear at 1236 and 1319 cm^{-1} in the spectra of PL, TBPL, and TFPL in Figure 1e, which can be ascribed to the new vibration mode generated by the hydrogen bond coupling between the -NH- vibration of the amide in the PL, TBPL, and TFPL and the —CF_3 groups in LiTFSI [40]. In addition, the symmetric bending vibration peak of the methyl groups on the ring of IPDI also shifts, which further confirms the presence of hydrogen bonding interactions between the urea bonds derived from —NHCONH— and the —CF_3 groups in Figure S5. All the above changes become more pronounced after the incorporation of Tp-TFMB. The results demonstrate that surface —CF_3-rich Tp-TFMB, effectively participating in and strengthening the entire interaction. It drives and preorganizes more anions into the trapping range of the PAMAM cage.

In addition, the hydrogen bond interaction can be reflected in the fluorescence signal via the differences in the microenvironment in the hyperbranched polyurea. Therefore, wavelength-resolved fluorescence imaging analysis is performed using confocal laser scanning microscopy (CLSM) to spatially resolve the dynamic reconstruction of the hydrogen bond network induced by the biomimetic "recognition–capture" strategy. As shown in the Figure 1f–i, the signal observed under excitation at 405 nm may be mainly derived from the intact and ordered amide/amine hydrogen bond clusters in the polymer backbone [41, 42]. In contrast, the enhanced signal under excitation at 488 nm may correspond to the sites where the hydrogen bond network is disturbed, and specific coordination with LiTFSI occurs or ionic aggregates are formed, thus representing potential ionic conductive microregions with strong ion-polymer interactions [43, 44]. As shown in Figure 1f,g, the clustered yet relatively uniform fluorescence signals in the PL polymer electrolyte. However, the fluorescence signal intensity is significantly enhanced, and its spatial distribution becomes extremely uniform in the TFPL composite electrolyte when Tp-TFMB is introduced. The distinct difference indicates that Tp-TFMB effectively drives and enriches more $TFSI^-$ anions around the PAMAM cages, thereby disturbing and reconstructing the original amide-based hydrogen bond network, and forming a large number of uniformly distributed regions with strong ion-polymer interactions. Meanwhile, the solid UV–vis diffuse reflectance spectroscopy (solid UV–vis) further confirms the above results in Figure S6. In the visible light region (400–600 nm), PL only exhibits weak background absorption with no characteristic peaks. After COF is introduced, TBPL shows weak absorption shoulders at 350 and 450 nm due to the structure of TpBd. Compared with TBPL, the absorption intensity of TFPL in the visible light region is significantly enhanced and red-shift. The phenomenon directly verifies that the strong electron-withdrawing —CF_3 reduces the electron cloud density and enhances the polarity of the COF conjugated backbone via the inductive effect [45]. The resulting Tp-TFMB improves interfacial compatibility with the PL polymer through interactions. Furthermore, the redshifted and broadened absorption band observed in TFPL provides spectroscopic evidence for the subsequent redistribution of $TFSI^-$ anions. Once repelled from the COF interface, these anions heterogeneously bind to amide cages at various sites within the PAMAM network, creating a diversity of local chemical environments that manifests as the observed absorption broadening.

Additionally, when the Tp-TFMB is added into the polymer electrolyte matrix, the stress of TFPL shown in Figure S7 is increased from 1.1 MPa to 1.27 MPa compared with that of PL. The result may be attributed to joint contribution of the interaction between Tp-TFMB and polymer electrolyte matrix, as well as the rigid skeletal structure of Tp-TFMB. Meanwhile, the TFPL electrolyte shows no significant mass loss at 300°C, demonstrating excellent thermal stability (Figure S8).

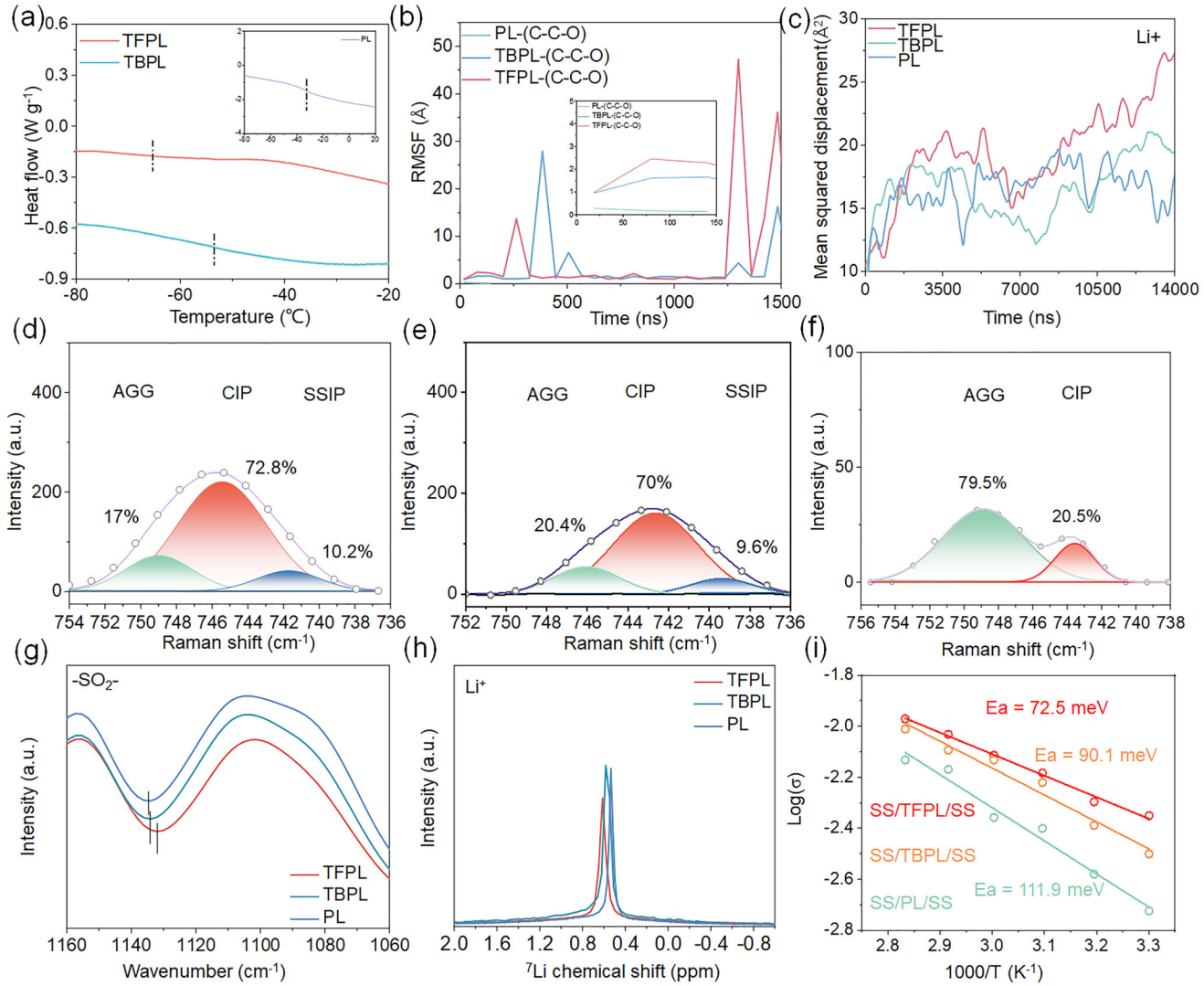

FIGURE 2 | (a) Differential scanning calorimetry (DSC) data of PL, TBPL, and TFPL; (b) DFT calculations of the mobility of C—C—O segments on PEA chains and (c) mean-square-displacement (MSD) of Li^+ based on PL, TBPL and TFPL; Raman spectra of (d) TFPL, (e) TBPL, and (f) PL; (g) FTIR and (h) ^7Li solid-state nuclear magnetic resonance (NMR) spectra of PL, TBPL, and TFPL; (i) Ionic conductivities at different temperatures and lithium-ion migration activation energies of PL, TBPL, and TFPL.

2.2 | Decoupled Ion Transport and Polymer Segmental Motion

Based on the biomimetic "recognition–capture" strategy, the TFPL electrolyte exhibits significantly enhanced polymer segment mobility and an optimized lithium-ion solvation structure, thereby synergistically facilitating the rapid transport of Li^+. As shown in Figure 2a, the introduction of TpBd and Tp-TFMB effectively suppresses the crystallization of polyether segments (—CH_2—CH_2—O—) and promotes amorphization of the electrolyte, resulting in the significant reduction in the glass transition temperature (T_g) of TBPL and TFPL compared with PL. Specifically, the T_g of TBPL is −53.7°C, and that of TFPL further decreases to -65.2°C, which is much lower than the T_g of PL (−29.1°C). Meanwhile, the DFT simulations in Figure 2b further confirm that the —CH_2—CH_2—O— on the PEA chains in the TFPL exhibit significantly larger motion amplitudes. The incorporation of COF disrupts the ordered arrangement of polyetheramine chains and increases the degree of freedom of segment motion [46].

Meanwhile, benefiting from the efficient anion management enabled by the biomimetic "recognition-capture" strategy, the large number of $TFSI^-$ anions are confined in the amide cages of PAMAM. This not only greatly promotes the dissociation of LiTFSI, but also optimizes the solvation structure of Li^+. As shown in Figure 2d–f, the Raman spectroscopy analysis reveals that the proportions of Li^+—$TFSI^-$ contact ion pairs (CIPs) and solvent-separated ion pairs (SSIPs) in the TFPL electrolyte are significantly enhanced. Specifically, the proportion of CIP increases further from 20.5% in PL and 70% in TBPL to 72.8% in TFPL, while the proportion of SSIP structures rises from 9.6% in TBPL to 10.2% in TFPL. Meanwhile, the proportion of ion aggregates (AGGs) drops sharply from 79.5% in PL and 20.4% in TBPL to 17%. The structural evolution directly confirms the more complete dissociation of the LiTFSI, where Li^+ are more coordinated with PEA, forming a solvation environment more conducive to rapid ion migration in TFPL. The FTIR spectroscopy and solid-state ^7Li nuclear magnetic resonance (NMR) spectroscopy further corroborate the above conclusions.

As shown in Figure 2g, the characteristic —SO_2— peak of $TFSI^-$ in TBPL and TFPL undergoes redshift (shifted to 1134.1 cm^{-1}) and further red-shift to 1132.2 cm^{-1} in TFPL compared with PL (1136 cm^{-1}). This indicates that Tp-TFMB, which repel anions and the amide which serves as the traps to capture anions, synergistically intensify the perturbation of the local anionic environment. In addition, the solid-state ^7Li NMR peak of TFPL exhibits a distinct downfield shift compared with those of PL and TBPL, which directly demonstrates that Li^+ possesses the strongest migration capability in the TFPL electrolyte, as shown in Figure 2h. Meanwhile, the calculations based on the MSD reveals that the mobility of $TFSI^-$ in the TFPL electrolyte is significantly lower than that in the PL and TBPL in Figure S9. The dynamic confinement phenomenon is directly verified by NMR spectroscopy; the characteristic peak of $TFSI^-$ in the ^{19}F NMR spectrum of TFPL exhibits a systematic high-field shift (Figure S10). The two independent pieces of evidence collectively confirm that the biomimetic "recognition–capture" strategy markedly restricts the migration ability of $TFSI^-$ anions via the efficient recognition and capture of $TFSI^-$ anions by fluorinated COFs. The combined effects of enhanced segment mobility and optimized solvation structure significantly reduce the energy barrier for lithium-ion transport. The stainless steel/TFPL/stainless steel (ss/TFPL/ss) cell shows lowest impedance (6.25 Ω). The TFPL electrolyte possesses the higher ionic conductivity of 4.5 mS cm^{-1} than TBPL (3.2 mS $^{-1}$cm) and PL (1.9 mS $^{-1}$cm) in Figures 2i and S15. Therefore, the ion migration activation energy (E_a) calculated based on the Arrhenius equation reveals that the value of the TFPL is as low as 72.5 meV. In contrast, the values of TBPL and the PL reach 90.1 and 111.9 meV, respectively, which further verifies the kinetic superiority of the biomimetic "recognition–capture" strategy from dynamic perspective.

2.3 | Interfacial Stability

Benefiting from the effective confinement of abundant $TFSI^-$ anions enabled by the biomimetic "recognition–capture" strategy, the t_{Li+} of TFPL is significantly enhanced and reached 0.7, which is notably higher than those of TBPL (0.42) and PL (0.24) in Figures 3a and S16. This indicates that the strategy successfully renders Li^+ the dominant charge carriers and thus markedly alleviates the concentration polarization. Additionally, the TFPL also significantly improves the transport and transfer resistance of Li^+ at the interface. In the assembled Li/TFPL/Li cell, the interfacial impedance is only 132.1 Ω and the charge transfer impedance is merely 39.6 Ω, which are much lower than those of the Li/TBPL/Li cell (197.7 Ω and 41.7 Ω) and the Li/PL/Li cell (218.1 Ω and 66.6 Ω).

Therefore, the strategy remarkably enhances the interfacial stability of lithium metal batteries. The Tafel tests performed on the assembled Li||Li symmetric cells show that the exchange current density of TFPL cell system is as high as 0.72 mA cm^{-2} in Figure 3b, outperforming those of TBPL cell system (0.54 mA cm^{-2}) and PL cell system (0.39 mA cm^{-2}), which implies faster interfacial charge transfer kinetics. Furthermore, the corrosion potential between TFPL and lithium metal is as low as 0.02 V, with a significant reduction compared with the PL and TBPL, demonstrating lower hindrance to the Li^+ deposition/stripping processes on the electrode surface and effective suppression of interfacial side reactions.

To further evaluate the interfacial compatibility between the electrolyte and electrodes, as well as the reversibility of lithium-ion deposition/stripping processes, Li||Cu cells and Li||Li cells are fabricated and subjected to long-term cycling. The test results demonstrate that the assembled Li/TFPL/Cu half-cell (Figure 3c) achieves a high average Coulombic efficiency (CE) of 96% and can cycle stably for 300 cycles, exhibiting excellent reversibility of lithium deposition and interfacial compatibility. In contrast, the CE of the Li/TBPL/Cu half-cell decays to 82.9% after 200 cycles, while that of the Li/PL/Cu half-cell drops sharply after merely 100 cycles. Concurrently, the Li/TFPL/Li symmetric cell shows no obvious voltage fluctuation or short-circuit signs at a current density of 1.2 mA cm^{-2} (Figure 3d). On the contrary, the Li/TBPL/Li and Li/PL/Li symmetric cells suffer premature short-circuit at current densities of 0.8 and 1.0 mA cm^{-2}, respectively, indicating insufficient interfacial uniformity and dendrite suppression capability. In terms of long-term cycling stability, the Li/TFPL/Li cell delivers a lower polarization voltage and can operate stably for more than 1800 h at a current density of 0.1 mA cm^{-2} (Figure 3e). In comparison, the Li/PL/Li cell shows a higher polarization voltage under the same conditions and fails after approximately 600 h, which proves that it lacks effective dendrite suppression and interfacial stabilization.

To further uncover the dynamic interfacial processes, the in-situ distribution of relaxation time (DRT) technology is employed to analyze the interfacial evolution during the charging process (Figure 3f–h). For the Li/TFPL/Li cell, the time constant related to interfacial impedance remains stable, while the time constant associated with charge-transfer impedance shows a trend of first increasing and then decreasing. This indicates that the formed SEI film possesses excellent adaptability and kinetic optimization capability, which facilitates the uniform deposition of lithium ions. In contrast, both the interfacial impedance and charge-transfer impedance of the Li/TBPL/Li cell increase continuously (Figure 4g), reflecting dynamic instability at the interface; meanwhile, the Li/PL/Li cell exhibits the largest interfacial impedance (Figure 4h), suggesting that it fails to form an effective stable interfacial layer.

2.4 | The Gradient-Distributed Interphase Layer

To clarify the critical role of Tp-TFMB in stabilizing the electrode/electrolyte interface, time-of-flight secondary ion mass spectrometry (TOF-SIMS) and x-ray photoelectron spectroscopy (XPS) are employed to conduct in-depth interfacial characterization of the cycled lithium metal anodes (Figures 4a–c and S19).

The characterization results consistently demonstrate that the incorporation of Tp-TFMB (TFPL) can significantly increase the content of LiF in the solid electrolyte interphase (SEI) and optimize the uniformity of its spatial distribution compared to TBPL and PL in Figure 1d,g,i Furthermore, XPS analysis exhibits a significantly enhanced characteristic LiF signal at 684.8 eV that can be detected on the surface of the lithium anode in the cycled Li/TFPL/Li cell in Figure 4e.

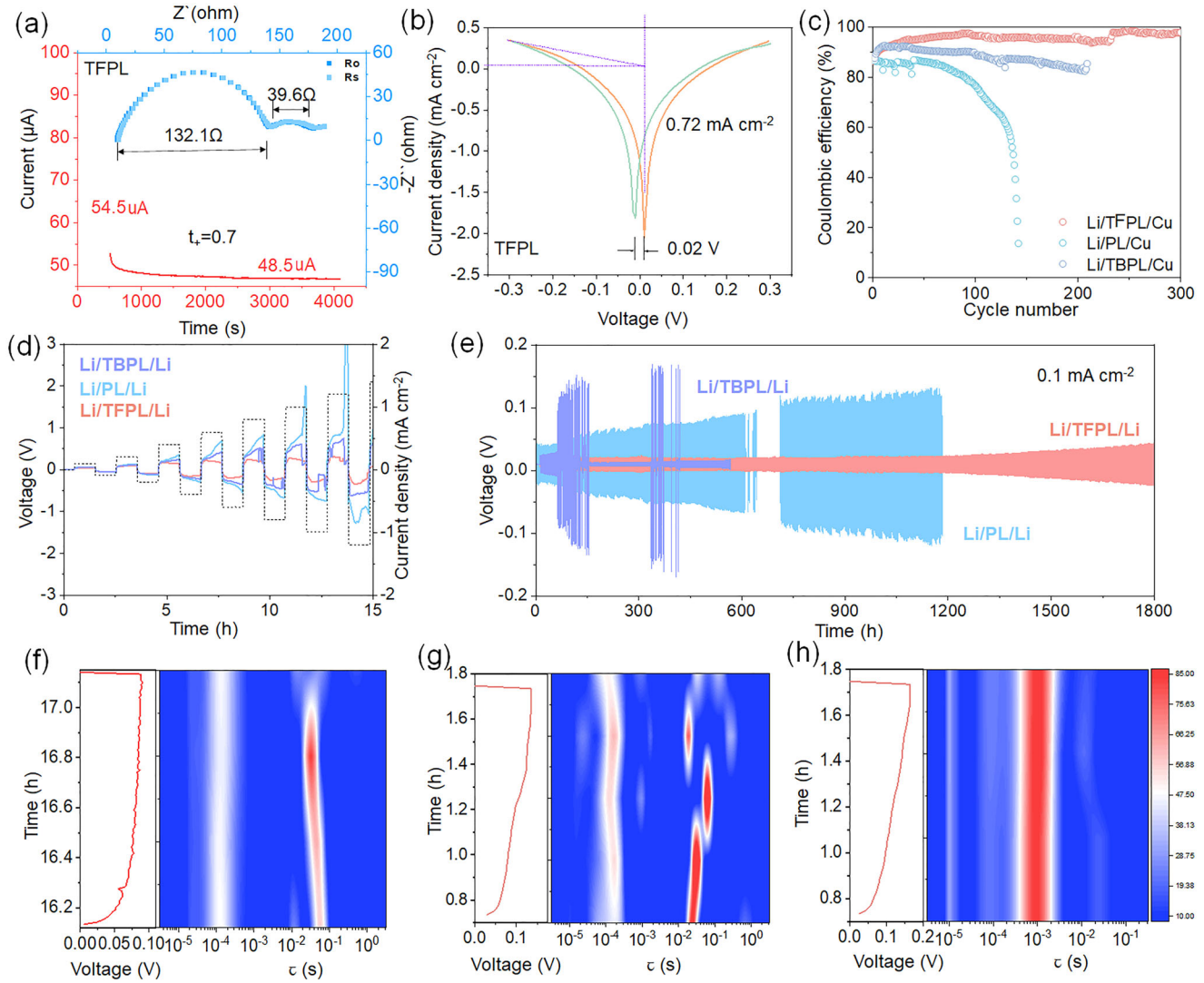

FIGURE 3 | (a) Lithium ion transference number of Li/TFPL/Li cell; (b) The Tafel plots of the assembled Li/TFPL/Cu cell; (c) Long-cycle performance of Li//Cu half-cells based on PL, TBPL, and TFPL at a current density of 0.1 mA cm−^{2}; (d) Limiting current densities of Li//Li half-cells based on PL, TBPL, and TFPL, and (e) their long-cycle performance at a current density of 0.1 mA cm−^{2}; (f) In-situ time relaxation distribution (TRD) tests of Li//Li half-cells based on TTPL, (g) TBPL, and (h) PL.

In contrast, the characteristic LiF signal is notably weaker on the anode surfaces of both the Li/TBPL/Li (Figure 4h) and Li/PL/Li (Figure 4k) cells. The result confirms that the TFPL electrolyte exhibits superior performance in constructing the LiF-rich interface. Furthermore, PAMAM-free PFCOF electrolyte is prepared and corresponding lithium symmetric cells are assembled. As shown in Figures S34a and 4k, LiF is detected on the lithium foil surfaces based on both PFCOF and PL electrolytes, while the cell based on PFCOF exhibits a significantly higher LiF signal intensity. These results indicate that Tp-TFMB promotes LiF accumulation and enables the formation of a stable interfacial layer. Further three-dimensional (3D) TOF-SIMS analysis clearly reveals that a gradient-ordered SEI structure is formed on the anode surface of the Li/TFPL/Li cell (Figure 4f): starting from the lithium metal side outward, the structure consists of an inner LiH layer to form LiF-LiH composite layer, an intermediate Li_2S layer, and an outer Li_3N layer, with highly abundant LiF uniformly dispersed throughout the entire SEI film. The layered structure forms a stable interphase layer enabling rapid lithium-ion transport [47]. In sharp contrast, the SEI formed in Li symmetric cells based on TBPL and PL electrolytes fails to develop such a well-defined layered architecture. Instead, it exhibits a disordered and incomplete distribution of key components in Figure 4i–l. The compositional chaos and the absence of a continuous, gradient structure directly indicate the failure to form a robust and stable interphase layer. Meanwhile, LiF species only locally accumulate on the upper surface of the Li foil in the PAMAM-free PFCOF cell in Figure S35a, while both TFPL5 (Figure S35b,e) and TFPL15 (Figure S35c,f) exhibit remarkably higher LiF content over the entire electrode surface. These results confirm that Tp-TFMB can effectively induce in-situ LiF formation, and the hyperbranched PAMAM structure further enriches interfacial LiF species to construct a more robust and uniform interphase layer. In terms of Li-N interfacial components, the Li/PFCOF/Li cell presents a very low Li—N signal (Figure S36a), whereas TFPL5 (Figure S36b) and TFPL15 (Figure S36c) possess abundant Li—N species, strongly demonstrating that the hyperbranched PAMAM skeleton is essential for the formation of Li—N interfacial products. In

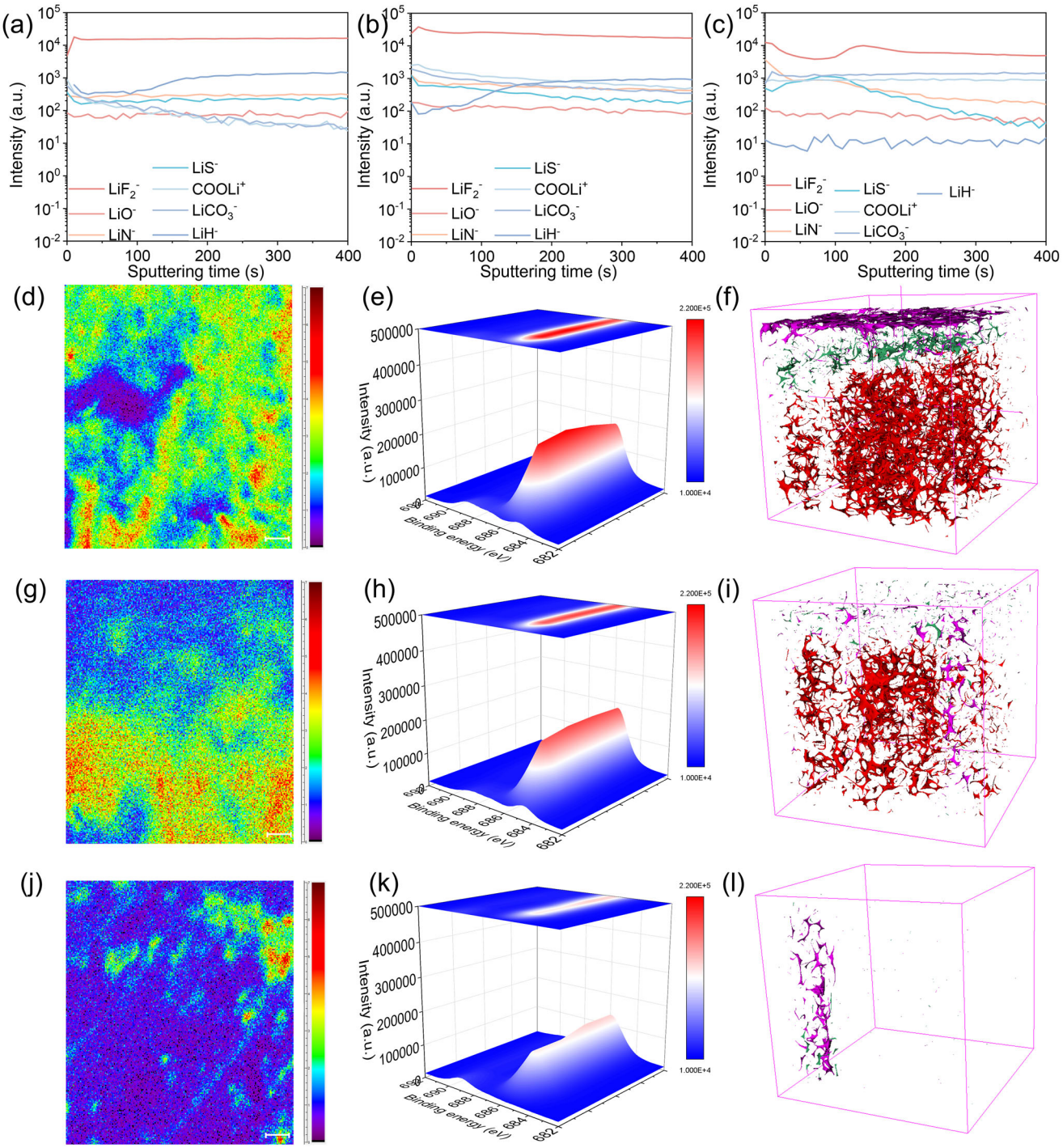

FIGURE 4 | (a) Depth profiling of lithium–metal surfaces based on Li/TFPL/Li, (b) Li/TBPL/Li, and (c) Li/PL/Li cells; 2D TOF-SIMS images of LiF^- on Li surfaces inside (d) Li/TFPL/Li, (g) Li/TBPL/Li, and (j) Li/PL/Li cells; 3D projection map of F spectrum in XPS based on the Li surface corresponding to (e) TFPL, (h) TBPL, and (k) PL; 3D TOF-SIMS elemental excluding LiF- distributions of (f) Li/TFPL/Li cell, (i)Li/TBPL/Li cell, and (l) Li/PL/Li cell.

addition, the PL electrolyte without Tp-TFMB yields only a small amount of Li—N components with extremely uneven distribution on the Li surface (Figure S21c). Collectively, these comparisons verify that the synergistic cooperation between Tp-TFMB and hyperbranched PAMAM significantly promotes the generation and uniform deposition of Li—N species, and only moderate Tp-TFMB loading achieves well-distributed Li—N interfacial structures.

The interfacial structure featuring high LiF content and ordered layered architecture acts as the fundamental microstructural basis for the superior cycling stability of the assembled batteries. This distinctive interfacial structural evolution can be directly attributed to the dynamic implementation of the biomimetic "recognition–capture" design strategy. Specifically, Tp-TFMB effectively repels and confines the $TFSI^-$ anions enriched on its surface within the amide "cages" of PAMAM. During

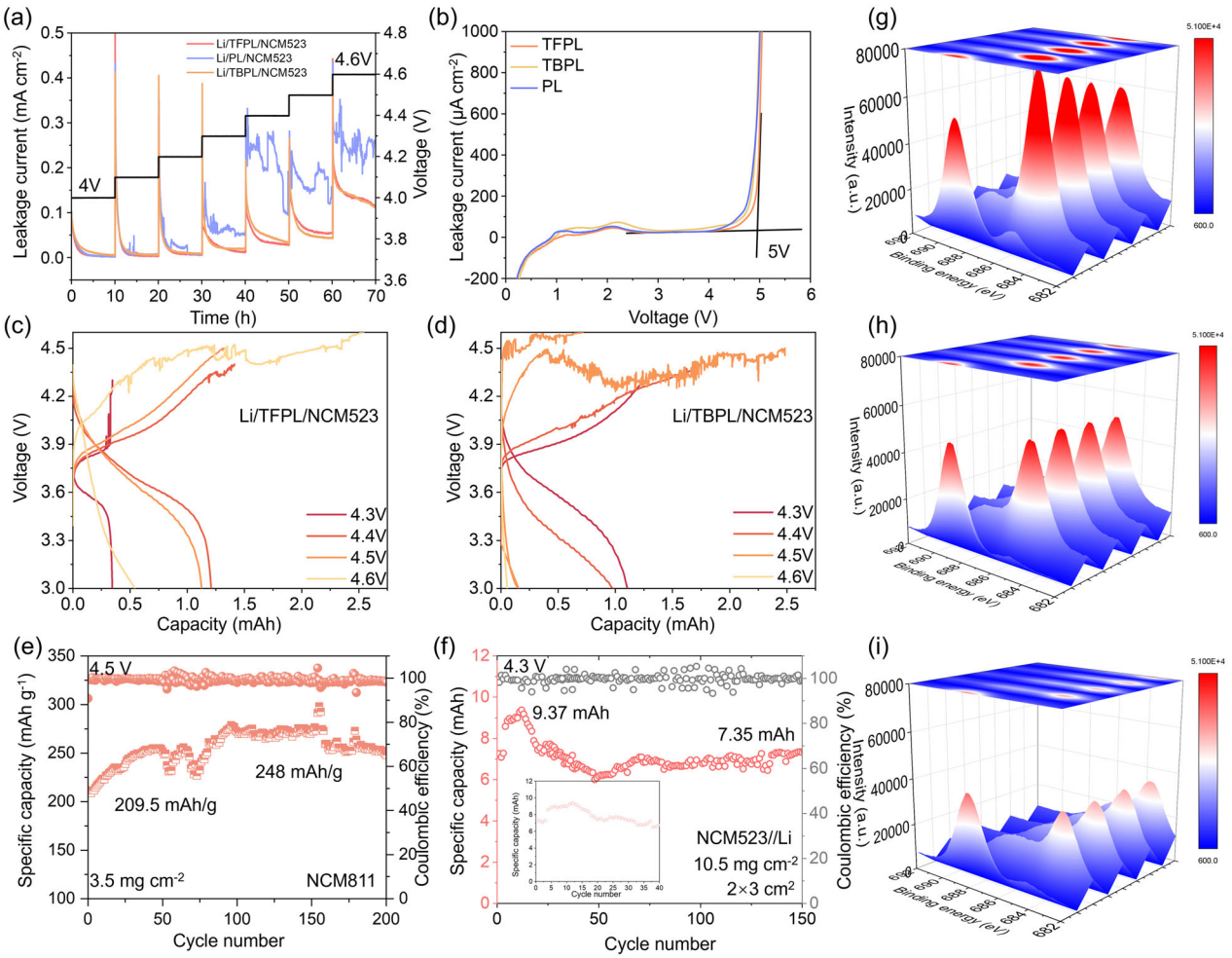

FIGURE 5 | (a) Electrochemical floating tests of Li//NCM523 cells based on PL, TBPL, and TFPL; (b) Linear sweep voltammetry tests of PL, TBPL, and TFPL; (c) Charge–discharge curves of Li/TFPL/NCM523 cells in the voltage range of 4.3–4.6 V; (d) Charge–discharge curves of Li/TBPL/NCM523 cells in the voltage range of 4.3–4.6 V. (e) Long-cycle performance of Li/TFPL/NCM811 cells at 0.1 C with an upper cut-off voltage of 4.5 V; (f) Long-cycle performance of high-loading NCM523 pouch cells based on TFPL at 0.1 C; 3D projection map of F spectrum in XPS based on the NCM523 surface corresponding to (g) TFPL, (h) TBPL, and (i) PL.

electrochemical cycling, these pre-enriched anions undergo orderly reduction: the S═O/S─N bonds break to form the intermediate Li_2S layer, while trace H^+ is reduced to generate the inner LiH layer. Most critically, the locally high-concentration fluorine sources (derived from the ─CF_3 groups of $TFSI^-$ and the Tp-TFMB) ensure the formation of a large quantity of uniformly distributed LiF in the final reduction state. These inorganic components collectively construct a stable gradient composite SEI structure.

2.5 | Compatibility With High-Voltage Cathodes

To investigate the effect of the biomimetic "recognition–capture" strategy on improving the cathode stability of composite electrolytes, systematic electrochemical characterizations are carried out. Constant–voltage floating charge tests performed at 4.1 and 4.6 V revealed that the leakage current of the Li/PL/NCM523 cell increases continuously, indicating severe electrolyte decomposition. In contrast, the Li/TBPL/NCM523 and Li/TFPL/NCM523 cells remained stable at the high voltage of 4.6 V, demonstrating that the interfacial side reactions are significantly suppressed (Figure 5a).

Further linear sweep voltammetry (LSV) tests reveal that the electrochemical stability window of the TFPL electrolyte is extended to 5.0 V (vs. Li/Li^+), confirming its excellent high-voltage tolerance (Figure 5b). To evaluate the practical application performance, full-cell tests of Li/NCM523 batteries are conducted at a high cut-off voltage of 4.5 V. The results show that the cell assembled with the TFPL electrolyte exhibits a stable charge–discharge profile and a discharge specific capacity of 1.17 mAh (Figure 5c). On the contrary, the cell assembled with the TBPL electrolyte exhibits voltage fluctuation and soft short-circuit (Figure 5d). Therefore, the cells based on the TFPL electrolyte exhibit excellent electrochemical performance under the conditions of NCM811 as cathode, 4.5 V cut-off voltage, and 0.1 C rate. Its initial discharge specific capacity reaches 209.5 mAh g^{-1}, and the capacity gradually climbs to a maximum of 248 mAh g^{-1} at 4.5 V. This may be due to the fact that in the early cycles, only surface NCM particles form efficient continuous Li^+ transport paths with the composite polymer solid electrolyte, while deep electrode active materials barely

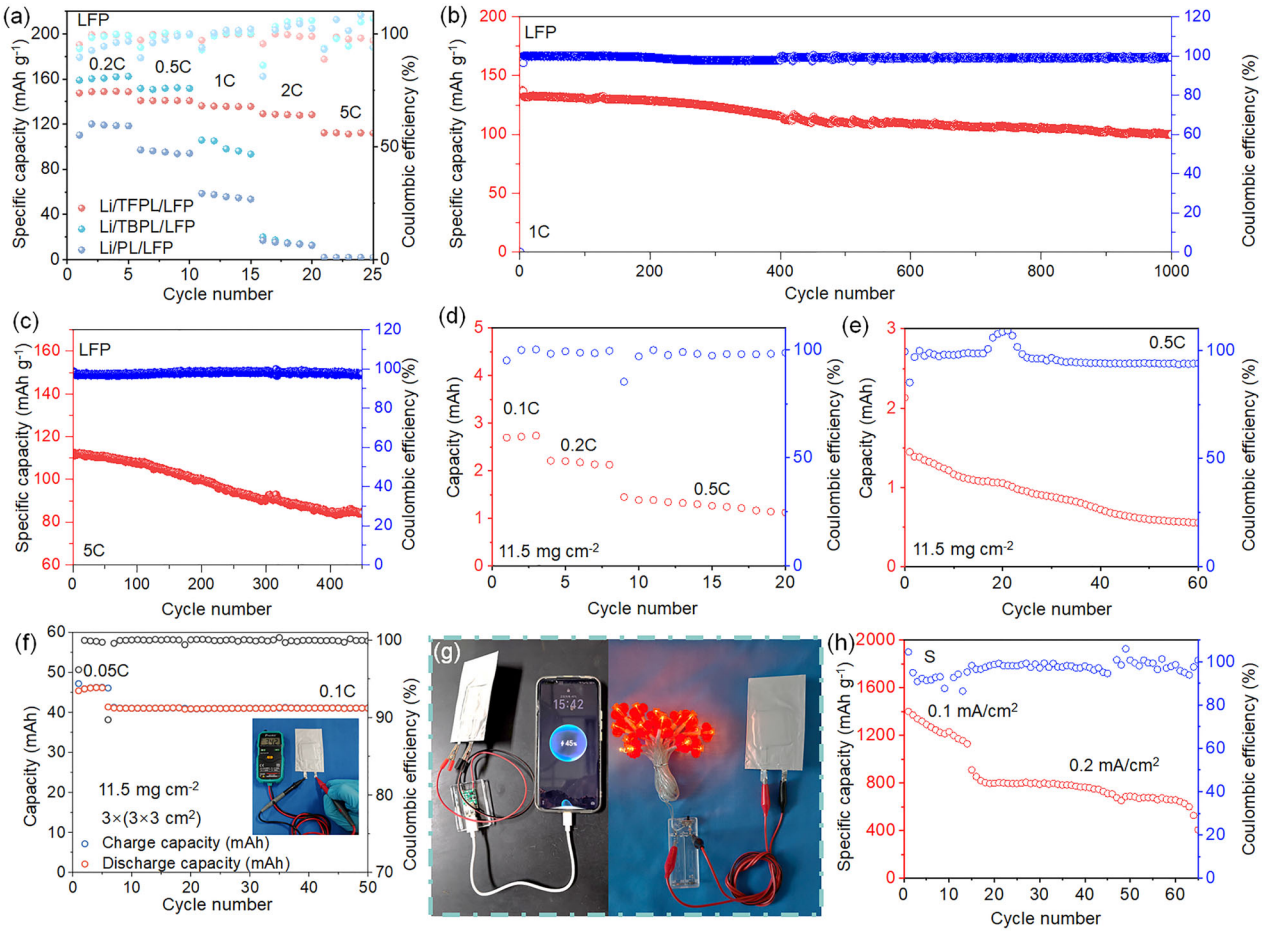

FIGURE 6 | (a) Rate performance of Li/LFP cells based on PL, TBPL, and TFPL at different rates; Long-cycle performance of Li/TFPL/LFP cells at (b) 1C and (c) 5C; (d) High load (11.5 mg/cm^2) LFP cell based on TFPL at different rate; (e) Long-cycle performance of high-loading LFP cells based on TFPL 0.5 C; (f) Long-cycle performance of the triple-layer high-loading LFP pouch cells based on TFPL, the inset figure shows the actual photograph of the pouch cell; (g) Triple-layer high-loading LFP pouch cell based on TFPL enables both mobile phone charging and small LED lamp illumination. (h) Cycling performance of Li/TFPL/S cells at different current densities.

engage in Li intercalation/deintercalation [48], resulting in lower the initial capacity. Constant reconstruction of uniform ion-conductive CEI interphases continuously activates inner inert active particles and steadily elevates discharge capacity [49]. Meanwhile, deep delithiation of NCM at 4.5 V induces severe lattice strain and internal stress [50], drastically raising interfacial impedance of inner particles without stable interphases and triggering violent capacity oscillation. After prolonged cycling, fully grown compact stable interphases stabilize solid-solid contact [51], gradually relieve capacity fluctuation. In addition, the pouch cells assembled with commercial NCM523 cathodes deliver a maximum discharge capacity of 9.37 mAh at 0.1 C, and still retain a high capacity of 6.73 mAh after 40 stable cycles. To investigate the interfacial advantages, the XPS characterization is performed on the surface of the cycled NCM523 cathodes. The results demonstrate that a significantly stronger characteristic LiF signal is detected on the cathode surface of the TFPL-based cell, confirming that the biomimetic "recognition-capture" strategy promotes the formation of a LiF-rich, structurally stable cathode electrolyte interphase (CEI). This effectively suppresses interfacial side reactions under high-voltage, resulting in the excellent cycling stability of the full cells.

2.6 | Long-Cycle Stability and Practical Applicability

To further verify the universality of the biomimetic "recognition–capture" strategy, the Li/TFPL/LFP cell is assembled and delivers discharge specific capacities of 149, 140.9, 135.7, 128.6, and 112.2 mAh g^{-1} at 0.2, 0.5, 1, 2, and 5 C, respectively (Figure 6a). Although the assembled Li/TBPL/LFP cells exhibit higher discharge specific capacities than Li/TFPL/LFP cells at 0.1 and 0.2 C, the capacity fades at higher rates. In contrast, the discharge specific capacities of the assembled Li/PL/LFP cells are significantly lower than those of TFPL-based LFP cells. For long-cycle testing at 1 C (Figure 6b), the Li/TFPL/LFP cell still retains a discharge specific capacity of 99.8 mAh g^{-1} after 1000 cycles, corresponding to the capacity retention rate of 75.5%. At 5 C, the Li/TFPL/LFP cell operates stably for 450 cycles with a high-capacity retention rate of 75.2% (Figure 6c). Importantly, the discharge capacity of the assembled high-loading Li/TFPL/LFP cell reaches 2.74 mAh at 0.1 C, 2.2 mAh at 0.2 C, and 1.45 mAh at 0.5 C (Figure 6d).

Furthermore, the cell operates stably for 20 cycles at 0.2 C with the discharge specific capacity of 1.82 mAh and 60 cycles at 0.5 C with

the discharge specific capacity of 1.5 mAh (Figure 6f). In contrast, the capacity of the Li/TBPL/LFP cell continuously fades to 0.7 mAh at 0.2 C. When assembled into triple-layer high-loading LFP/Li pouch cells, the Li/TFPL/LFP configuration delivers a maximum discharge capacity of 46.1 mAh at 0.05 C and 41.3 mAh at 0.1 C. Notably, the pouch cell maintains stable operation over 50 cycles at 0.1 C with nearly 100% capacity retention. In addition, the assembled triple-layer pouch cells are capable of charging smartphones shown in video and illuminating LED lamps successfully in Figure 6g, which provides intuitive evidence for their practical power delivery performance and promising application prospects. Finally, the Li/TFPL/S cell is assembled to further expand the application potential and the Li/TFPL/S cell delivers discharge specific capacities of 1401 and 909.8 mAh g^{-1} at current densities of 0.1and 0.2 mA cm^{-2}, respectively. Especially, the assembled cells retain the capacity of 659 mAh g–^{1} after 45 cycles 0.2 mA cm–^{2}. Reproducible measurements can be achieved for all batteries assembled with TFPL composite electrolyte. Minor performance disparities between different cells mainly stem from manual operational deviations during cell assembly. The battery curves display in all figures correspond to the sample with optimal cycling performance among parallel replicates. It is thus clear that the prepared composite polymer electrolyte TFPL demonstrates the good potential for application in various high-energy-density batteries.

3 | Conclusion

The biomimetic "recognition–capture" strategy is proposed to break the traditional dilemma in solid polymer electrolytes. The approach led to the successful fabrication of the TFPL based on hyperbranched PAMAM, PEA, and the fluorinated COF (Tp-TFMB). Among them, the Tp-TFMB directionally regulate $TFSI^-$ anions, while the PAMAM serves as the "cage" for their confinement. Consequently, the TFPL electrolyte achieves a high room-temperature ionic conductivity of 4.5 mS cm–^{1} and an elevated Li^+ transference number of 0.7. More importantly, this strategy in-situ induces the formation of a gradient, robust solid electrolyte interphase (Li_3N—Li_2S—LiF/LiH). The unique interfacial structure enables exceptionally stable lithium plating/stripping, evidenced by the Li//Li symmetric cell cycling over 1800 h and the Li//Cu half-cell maintaining high Coulombic efficiency of 96% for 300 cycles. The TFPL electrolyte also exhibits a wide electrochemical window up to 5.0 V (vs. Li/Li^+), demonstrating excellent compatibility with high-voltage NCM811 (4.5 V), LFP (5 C, 450 cycles), NCM523 (9.37 mAh), and sulfur cathodes. The assembled multi-layer LFP pouch cells deliver high discharge capacities (41.3 mAh) and stable cycling performance (50 cycles). This work provides a new paradigm for designing high-performance solid-state electrolytes through multi-component synergistic management, opening a promising avenue toward safe, high energy density lithium–metal batteries.

Author Contributions

Jiazhu Guan: data curation, methodology, conceptualization, investigation, writing – original draft, validation. **Yu Zhang**: validation, methodology. **Yong Cao**: resources. **Yajuan Zhou**: resources. **Wenping Liu**: resources. **Qinghui Zeng**: resources. **Zhengyan Lun**: resources. **Wei Cui**: validation, software. **Shi Wang**: writing – review and editing, resources. **Wei Liu**: funding acquisition, resources. **Zhong Jin**: writing – review and editing, resources. **Liaoyun Zhang**: funding acquisition, writing – review and editing, supervision.

Acknowledgments

This work was supported by the Key Project of National Natural Science Foundation of China (No. 12535018, U25A20628, 22561160129, 22479074, 22475096, 62288102, 52533008), the National Natural Science Foundation of China (52073285, 11975238), the Foundation Research Funds for the Central Universities and Nanjing University International Collaboration Initiative (020514380354), the National Key Research and Development Program of China (2024YFA1509400), the State Key Laboratory of Flexible Electronics Key Task Research Project (ZS030ZR25012), the Equipment Pre-Research and Ministry of Education Joint Fund (8091B02052407), the Fundamental Research Program Key Project of Jiangsu Province (BK20253008), the Science and Technology Major Project of Jiangsu Province (BG2024013), the Scientific and Technological Achievements Transformation Special Fund of Jiangsu Province (BA2023037), the Academic Degree and Postgraduate Education Reforming Project of Jiangsu Province (JGKT24_C001), the Key Core Technology Open Competition Project of Suzhou City (SYG2024122), the Open Research Fund of Suzhou Laboratory (SZLAB-1308-2024-TS005), and the Chenzhou National Sustainable Development Agenda Innovation Demonstration Zone Provincial Special Open Competition Project (2023sfq11, 2025sfq38), the Natural Science Foundation of NJUPT (NY223079, NY224119) The authors also thank for the help from the analysis and testing center at the University of Chinese Academy of Sciences.

Conflicts of Interest

The authors declare that they have no competing interests.

Data Availability Statement

The data that support the findings of this study are available from the corresponding author upon reasonable request.

References

1. S. Liu, L. Zhou, H. Li, and K. Neyts, "Novel Insights Into Solid-State Batteries Through Phase Modulations: Dielectric Phase and Liquid Crystal Phase," *Advanced Materials* 38 (2026): e17122, https://doi.org/10.1002/adma.202517122.

2. J. B. Waugh, M. Redko, X. Jin, et al., "Overcoming Misconceptions in Lithium Metal Polymer Electrolyte Batteries," *Energy & Environmental Science* 18 (2025): 9312–9323, https://doi.org/10.1039/D5EE03530A10.1039/D5EE03530A.

3. M.-H. Kim, J. Kim, S. H. Choi, et al., "Mitigating Electrode-Level Heterogeneity Using Phosphorus Nanolayers on Graphite for Fast-Charging Batteries," *ACS Energy Letters* 8 (2023): 3962–3970, https://doi.org/10.1021/acsenergylett.3c01134.

4. Y. B. Gao, W. L. Li, X. Chen, et al., "A Universal Principle of Lithium Bond Characteristics in Lithium Battery Electrolytes," *Angewandte Chemie International Edition* 65 (2026): e17523, https://doi.org/10.1002/anie.202517523.

5. Y. Han, Y. Chen, T. Zhang, et al., "Ether-Anchored MOFs Enable Stable Pseudosuspension Electrolytes for High-Energy Lithium Metal Batteries," *Angewandte Chemie International Edition* 64 (2025): e202518384, https://doi.org/10.1002/anie.202518384.

6. M.-H. Kim, D. Y. Kim, Y. Li, et al., "Horizontal Lithium Growth Driven by Surface Dynamics on Single Crystal Cu(111) Foil," *Energy & Environmental Science* 17 (2024): 6521–6532, https://doi.org/10.1039/D4EE01766H.

7. M.-H. Kim, T. U. Wi, J. Seo, et al., "Design Principles for Fluorinated Interphase Evolution via Conversion-Type Alloying Processes for Anticor-

rosive Lithium Metal Anodes," *Nano Letters* 23 (2023): 3582–3591, https://doi.org/10.1021/acs.nanolett.3c00764.

8. S. Wang, S. Xiao, S. Li, et al., "Organic Cationic-Coordinated Perfluoropolymer Electrolytes With Strong Li^+-Solvent Interaction for Solid State Li-Metal Batteries," *Angewandte Chemie International Edition* 63 (2024): e202412434, https://doi.org/10.1002/anie.202412434.

9. S. Wang, L. Zhang, Z. Hu, et al., "Intrinsic Structural and Coordination Chemistry Insights of Li Salts in Rechargeable Lithium Batteries," *Advanced Materials* 37 (2025): 2420428, https://doi.org/10.1002/adma.202420428.

10. Y. Jiang, L. Liu, Y. Liu, et al., "A Novel Orientation Aliphatic Ketone-Based Liquid Crystal Polymer Electrolyte for High-Voltage Solid-State Lithium Metal Batteries," *Advanced Functional Materials* 35 (2025): 2502613, https://doi.org/10.1002/adfm.202502613.

11. J. Guan, X. Li, L. Zhou, et al., "Enabling Fast-Charging Capability of High-Voltage Solid-State Lithium Metal Batteries by In-Situ Composite of COF Into Polymer Electrolyte," *Chemical Engineering Journal* 516 (2025): 164071, https://doi.org/10.1016/j.cej.2025.164071.

12. T. Zhang, K. Huang, Y. Zheng, et al., "Loss and Recovery of Effective Lithium in Anode-Free Solid-State Lithium Metal Batteries," *Advanced Materials* 37 (2025): e05695, https://doi.org/10.1002/adma.202505695.

13. D.-H. Guan, X. X. Wang, L. Li, G. N. Chen, G.-Y. Qiao, and J.-J. Xu, "Homologous Imide Bonds to Build Polymer-Covalent Organic Framework Electrolytes for Efficient Ion Transport," *Journal of the American Chemical Society* 147 (2025): 38078–38088, https://doi.org/10.1021/jacs.5c09639.

14. T. Xiao, J. Xian, Z. Yu, et al., "Cationic–Zwitterionic Polymer Electrolytes With Enhanced Ionic Conductivity and Lithium-Ion Selectivity for Solid-State Batteries," *Angewandte Chemie International Edition* 64 (2025): e202514027, https://doi.org/10.1002/anie.202514027.

15. Z. Huang, Z. Wang, X. Chen, et al., "Interface Engineering and Optimization Strategies for High-Energy-Density Batteries Based on Polymer Composite Electrolytes," *Advanced Materials* 37 (2025): e04186, https://doi.org/10.1002/adma.202504186.

16. H. An, M. Li, Q. Liu, et al., "Strong Lewis-Acid Coordinated PEO Electrolyte Achieves 4.8 V-Class All-Solid-State Batteries Over 580 Wh Kg^{-1}," *Nature Communications* 15 (2024): 9150, https://doi.org/10.1038/s41467-024-53094-8.

17. W. Zhang, V. Koverga, S. Liu, et al., "Single-phase Local-High-Concentration Solid Polymer Electrolytes for Lithium-Metal Batteries," *Nature Energy* 9 (2024): 386–400, https://doi.org/10.1038/s41560-023-01443-0.

18. A. Chen, Q. Zeng, W. Wen, et al., "A Highly Salt-Soluble Ketone-Based All-Solid-State Polymer Electrolyte With Superior Performances for Lithium-Ion Batteries," *ACS Applied Materials & Interfaces* 15 (2023): 17791–17800, https://doi.org/10.1021/acsami.2c22228.

19. O. Sheng, X. Li, T. Yang, et al., "Solid Polymer Electrolyte Chemistries Tailored by Solvation Structures," *eScience* 6 (2025): 100504, https://doi.org/10.1016/j.esci.2025.100504.

20. J. Zhu, P. Bian, G. Sun, et al., "Practical High-Voltage Lithium Metal Batteries Enabled by the In-Situ Fabrication of Main-Chain Fluorinated Polymer Electrolytes," *Angewandte Chemie International Edition* 64 (2025): e202424685, https://doi.org/10.1002/anie.202424685.

21. Y. Wang, Z. Wu, F. M. Azad, et al., "Fluorination in Advanced Battery Design," *Nature Reviews Materials* 9 (2024): 119–133, https://doi.org/10.1038/s41578-023-00623-4.

22. D. Okuda, M. Deguchi, S. Yamazaki, and M. Ishikawa, "Mechanism of Polysulfide Dissolution Suppression in Lithium-Sulfur Batteries Using a Novel Fluorinated Ether Electrolyte," *Electrochimica Acta* 572 (2026): 149154, https://doi.org/10.1016/j.electacta.2026.149154.

23. X. Xiong, Y. Peng, Y. Chen, et al., "A Rational Roadmap for Electrolyte Additives in High-Energy Lithium-Metal Batteries," *Progress in Materials Science* 162 (2026): 101730, https://doi.org/10.1016/j.pmatsci.2026.101730.

24. J. R. Nair, L. Porcarelli, F. Bella, and C. Gerbaldi, "Newly Elaborated Multipurpose Polymer Electrolyte Encompassing RTILs for Smart Energy-Efficient Devices," *ACS Applied Materials & Interfaces* 7 (2015): 12961–12971, https://doi.org/10.1021/acsami.5b02729.

25. F. Elizalde, J. Amici, S. Trano, et al., "Self-healable Dynamic Poly(Urea-Urethane) Gel Electrolyte for Lithium Batteries," *Journal of Materials Chemistry A* 10 (2022): 12588–12596, https://doi.org/10.1039/D2TA02239G.

26. F. Pei, Y. Huang, L. Wu, et al., "Multisite Crosslinked Poly(Ether-Urethane)-Based Polymer Electrolytes for High-Voltage Solid-State Lithium Metal Batteries," *Advanced Materials* 36 (2024): 2409269, https://doi.org/10.1002/adma.202409269.

27. Y. Ye, X. Zhu, N. Meng, and F. Lian, "Largely Promoted Mechano-Electrochemical Coupling Properties of Solid Polymer Electrolytes by Introducing Hydrogen Bonds-Rich Network," *Advanced Functional Materials* 33 (2023): 2307045, https://doi.org/10.1002/adfm.202307045.

28. C. Fu, G. Homann, R. Grissa, et al., "A Polymerized-Ionic-Liquid-Based Polymer Electrolyte With High Oxidative Stability for 4 and 5 V Class Solid-State Lithium Metal Batteries," *Advanced Energy Materials* 12 (2022): 2200412, https://doi.org/10.1002/aenm.202200412.

29. Y. Li, Y. Liu, L. Xue, et al., "Eliminating Anion Depletion Region and Promoting Li^+ Solvation via Anionphilic Metal Organic Framework for Dendrite-Free Lithium Deposition," *Nano Energy* 92 (2022): 106708, https://doi.org/10.1016/j.nanoen.2021.106708.

30. L. Huang, Y. Wu, M. Li, et al., "Side-chain Engineering of Fluorinated Gel Polyester Electrolyte Enabling Fast-Charging and High-Loading Li Metal Batteries," *Materials Today* 91 (2025): 176–185, https://doi.org/10.1016/j.mattod.2025.11.016.

31. T. U. Wi, S. O. Park, S. J. Yeom, et al., "Revealing the Dual-Layered Solid Electrolyte Interphase on Lithium Metal Anodes via Cryogenic Electron Microscopy," *ACS Energy Letters* 8 (2023): 2193–2200, https://doi.org/10.1021/acsenergylett.3c00505.

32. Y. Cui, J. Liu, H. Wang, M. Zhang, and H. Wang, "Electrochemical Oscillatory Screening Anion to Form LiF-Rich SEI for Enhanced Stability of Silicon Anode," *Small* 21 (2025): e09381, https://doi.org/10.1002/smll.202509381.

33. Y. Wang, Z. Wang, L. Zhao, et al., "Lithium Metal Electrode With Increased Air Stability and Robust Solid Electrolyte Interphase Realized by Silane Coupling Agent Modification," *Advanced Materials* 33 (2021): 2008133, https://doi.org/10.1002/adma.202008133.

34. T. Krauskopf, F. H. Richter, W. G. Zeier, and J. Janek, "Physicochemical Concepts of the Lithium Metal Anode in Solid-State Batteries," *Chemical Reviews* 120 (2020): 7745–7794, https://doi.org/10.1021/acs.chemrev.0c00431.

35. W.-Z. Huang, C.-Z. Zhao, P. Wu, et al., "Anode-Free Solid-State Lithium Batteries: A Review," *Advanced Energy Materials* 12 (2022): 2201044, https://doi.org/10.1002/aenm.202201044.

36. P. Dong, X. Zhang, W. Hiscox, et al., "Toward High-Performance Metal–Organic-Framework-Based Quasi-Solid-State Electrolytes: Tunable Structures and Electrochemical Properties," *Advanced Materials* 35 (2023): 2211841, https://doi.org/10.1002/adma.202211841.

37. N. Meng, Y. Ye, Z. Yang, H. Li, and F. Lian, "Developing Single-Ion Conductive Polymer Electrolytes for High-Energy-Density Solid State Batteries," *Advanced Functional Materials* 33 (2023): 2305072, https://doi.org/10.1002/adfm.202305072.

38. H. P. Liang, M. Zarrabeitia, Z. Chen, et al., "Polysiloxane-Based Single-Ion Conducting Polymer Blend Electrolyte Comprising Small-Molecule Organic Carbonates for High-Energy and High-Power Lithium-Metal Batteries," *Advanced Energy Materials* 12 (2022): 2200013, https://doi.org/10.1002/aenm.202200013.

39. Y. Wang, S. Zhang, Z. Chen, et al., "Long-Life Lithium Metal Batteries Enabled by In Situ Solidified Polyphosphoester-Based Electrolyte," *Advanced Materials* 38 (2026): e14210, https://doi.org/10.1002/adma.202514210.

40. F. Zhen, H. Liu, Y. Wu, et al., "The Spontaneous Cascade Optimization Strategy of the Double Enrichment Improves Anion-Derived Solid Electrolyte Interphases to Enable Stable Lithium-Metal Batteries," *Energy & Environmental Science* 18 (2025): 4690–4703, https://doi.org/10.1039/D5EE01219H.

41. Z. Dong, Y. Bi, H. Cui, et al., "AIE Supramolecular Assembly With FRET Effect for Visualizing Drug Delivery," *ACS Applied Materials & Interfaces* 11 (2019): 23840–23847, https://doi.org/10.1021/acsami.9b04938.

42. G. Zhang, F. Mo, L. Song, et al., "Cluster-Dominated Electrochemiluminescence of Tertiary Amines in Polyethyleneimine Nanoparticles: Mechanism Insights and Sensing Application," *Analytical Chemistry* 94 (2022): 14682–14690, https://doi.org/10.1021/acs.analchem.2c03033.

43. R. Konefał, Z. Morávková, B. Paruzel, et al., "Effect of PAMAM Dendrimers on Interactions and Transport of LiTFSI and NaTFSI in Propylene Carbonate-Based Electrolytes," *Polymers* 12 (2020): 1595, https://www.mdpi.com/2073-4360/12/7/1595.

44. Z. Zhao, F. Li, J. Zhao, et al., "Ionic-Association-Assisted Viscoelastic Nylon Electrolytes Enable Synchronously Coupled Interface for Solid Batteries," *Advanced Functional Materials* 30 (2020): 2000347, https://doi.org/10.1002/adfm.202000347.

45. S. Suleman, Y. Zhang, Y. Qian, et al., "Turning on Singlet Oxygen Generation by Outer-Sphere Microenvironment Modulation in Porphyrinic Covalent Organic Frameworks for Photocatalytic Oxidation," *Angewandte Chemie International Edition* 63 (2024): e202314988, https://doi.org/10.1002/anie.202314988.

46. S. E. Neumann, J. Kwon, C. Gropp, et al., "The Propensity for Covalent Organic Frameworks to Template Polymer Entanglement," *Science* 383 (2024): 1337–1343, https://www.science.org/doi/abs/10.1126/science.adf2573.

47. X. Liu, S. Li, C. Yuan, et al., "Probing the Heterogeneous Nature of LiF in Solid–Electrolyte Interphases," *Nature* 646 (2025): 102–107, https://doi.org/10.1038/s41586-025-09498-7.

48. X. Luo, Z. Chen, X. Qiu, and Y. Qian, "Structure and Interfacial-Stable Binder Engineering Enables High-Rate Capability of NCM811 Cathodes at 4.6 V," *Advanced Energy Materials* 16 (2026): e70842, https://doi.org/10.1002/aenm.70842.

49. J. Mi, J. Yang, L. Chen, et al., "A Ductile Solid Electrolyte Interphase for Solid-State Batteries," *Nature* 647 (2025): 86–92, https://doi.org/10.1038/s41586-025-09675-8.

50. Z. Liu, Y. Zeng, J. Tan, et al., "Revealing the Degradation Pathways of Layered Li-Rich Oxide Cathodes," *Nature Nanotechnology* 19 (2024): 1821–1830, https://doi.org/10.1038/s41565-024-01773-4.

51. Z. Yao, Z. Liu, K. Xia, et al., "Design and Preparation of Self-Adaptive and Robust Solid-State Elastomeric Electrolyte for Lithium Metal Battery Inspired by Rubber Tire," *Angewandte Chemie International Edition* 64 (2025): e202513167, https://doi.org/10.1002/anie.202513167.

Supporting Information

Additional supporting information can be found online in the Supporting Information section.

Supporting File 1: anie73913-sup-0001-SuppMat.docx.

Supporting File 2: anie73913-sup-0002-VideoS1.mp4.